2024

Application of a scale resolving turbulence model to a jet in supersonic crossflow

Noah Schwalb

Recommended Citation

Schwalb, Noah, "Application of a scale resolving turbulence model to a jet in supersonic crossflow" (2024). *Theses*. 657.
https://louis.uah.edu/uah-theses/657

APPLICATION OF A SCALE RESOLVING TURBULENCE MODEL TO A JET IN SUPERSONIC CROSSFLOW

Noah Schwalb

A THESIS

Submitted in partial fulfillment of the requirements
for the degree of Master of Science
in
The Department of Mechanical and Aerospace Engineering
to
The Graduate School
of
The University of Alabama in Huntsville

May 2024

Approved by:

Dr. Abdelkader Frendi, Research Advisor/Committee Chair
Dr. Sarma Rani, Committee Member
Dr. Sivaguru Ravindran, Committee Member
Dr. George Nelson, Department Chair
Dr. Shankar Mahalingam, College Dean
Dr. Jon Hakkila, Graduate Dean

Abstract

APPLICATION OF A SCALE RESOLVING TURBULENCE MODEL TO A JET IN SUPERSONIC CROSSFLOW

Noah Schwalb

**A thesis submitted in partial fulfillment of the requirements
for the degree of Master of Science**

Mechanical and Aerospace Engineering

The University of Alabama in Huntsville
May 2024

The Partially-Averaged Navier-Stokes (PANS) methodology is applied to variable-density flow to derive the Blended PANS (BPANS) model. A supersonic jet-in-crossflow problem is numerically simulated using the BPANS model to show its capabilities in a variable-density flow with complex physics. The shock systems and vortex structures of this problem observed during experiments are numerically reproduced. The time-averaged Mach number and streamwise velocity contours show good agreement compared to LES and experimental data. The streamwise and wall-normal velocity profiles, wall pressure distribution along the flat plate, and trajectory of the jet are compared to LES and experimental data to show that BPANS accurately predicts them. The filter control parameter f_k is varied to show the effect of the unresolved to resolved ratio of the turbulent kinetic energy k and the specific dissipation rate ω. The results show that smaller f_k results in better agreement with LES and experimental data near local extrema.

Acknowledgements

I would like to thank my family, friends, and the UAH Ultimate Frisbee team for providing the support and encouragement that has allowed me to make it through graduate school. I would also like to thank my partner Emma for being a rubber ducky when I needed it, and keeping me grounded during the toughest days. Lastly, none of this work would have been possible without my advisor Dr. Frendi, who has guided me through graduate school with endless academic advice and directed me through the research process.

Table of Contents

List of Figures

Chapter 1. Introduction

Many engineering design problems involve some form of turbulent flow. It affects many aspects of a design, including the wings of an aircraft, the flow through an axial compressor, or even the combustion of fuel and oxidizer in an engine. One specific problem that involves turbulent flow is the high speed jet in crossflow (JICF). This is relevant to supersonic combustors, where the mixing of fuel and air is critical to the combustion process. A detailed understanding of the physics and accurate prediction of the turbulent mixing mechanisms is essential for combustor design.

A review paper by Mahesh covers the previous work done on high speed jets in crossflows [5]. Many recent studies are motivated by the application of high speed JICF to supersonic combustion. Some studies are experimental and include techniques such as Schlieren photography [24] [32], laser-induced fluorescence [20] [21] [1], and particle image velocimetry (PIV) [4] [2] [6] [3]. Flow measurements are very difficult for this type of flow due to the complexity of the flow physics. As a result, flow visualization has been used to study the turbulent mixing of the jet, the penetration of the jet, as well as the overall flow physics and shock structures.

Some vortical and shock structures have been identified as key features in a high speed JICF. There is a separation region just upstream of the jet due to the jet blocking the supersonic crossflow, along with a bow shock just upstream of that separation. The separation region lifts the boundary layer from the wall, creating a separation shock just ahead of the aforementioned bow shock [14] [32]. There is also an inclined barrel shock and a Mach disk at the boundary of the jet plume as it exits the nozzle, which interacts with the crossflow. The vortical structures that appear are similar to a low speed JICF: jet shear layer vortices, downstream wake vortices, horseshoe vortices that wrap around the jet column, and the counter-rotating vortex pair (CVP) far downstream. Fric and Roshko [10] note that the horseshoe vortices and CVP are usually observed in the mean flow and have unsteady components, while the shear layer and downstream wake vortices are inherently unsteady.

Turbulence is chaotic by nature, causing a net increase in mixing within the fluid and transferring more momentum, heat, and species concentration throughout a flow [30]. The first to observe a transition from laminar to turbulent flow was Reynolds [27], who experimentally investigated the subject by injecting dye into a pipe flow. Through his experiments, he characterized the transition of a flow from laminar to turbulent using a nondimensional number that has hence been named after him: the Reynolds number [27]. He later attempted to tackle the problem of turbulence theoretically by averaging the Navier-Stokes equations to solve for the mean flow quantities. It is unfortunate that these Reynolds-Averaged Navier Stokes (RANS) equations introduce new stress terms that contain more unknowns than there are equations. These terms are fittingly named the Reynolds stresses and must be modeled in order to close the RANS equations and obtain a solution.

Boussinesq tackled this challenge by introducing the idea of an eddy viscosity [33], which models the transport of the Reynolds stresses similar to the viscosity transporting the momentum of a fluid. It is a quantity that is formed such that it may be written as the product of a length and velocity scale. Prandtl built on this concept in the form of a mixing length model (a one-equation model) [31], where the eddy viscosity is proportional to the mean velocity gradient and a mixing length squared. This length scale requires a-priori knowledge of the flow geometry and thus is a major disadvantage of the model. Kolmogorov proposed the first two-equation model, where the turbulent kinetic energy and turbulent frequency are obtained using a transport equation for each variable [36]. Others have built on this concept, with the $(k-\epsilon)$ model [17] being developed to solve for the turbulent kinetic energy and turbulent dissipation. Wilcox developed another model called the $(k-\omega)$ model [41] due to the poor performance of the $(k-\epsilon)$ model near the wall, which did yield improved predictions as intended [42]. It is important to note, however, that the $(k-\omega)$ model is extremely sensitive to the freestream turbulence boundary conditions, which can significantly impact the results [22]. Menter built on the benefits of those two-equation models by blending them together, reducing to a form that is equivalent to $(k-\omega)$ near the wall and $(k-\epsilon)$ far from the wall [22].

These models fail to capture the unsteady, three-dimensional turbulent structures due to Reynolds-Averaging over all scales. Other methods are capable of resolving the turbulent motions within a flow at a much higher computational cost such as Direct Numerical Simulation (DNS). It works as the name suggests: the full Navier-Stokes equations are solved without models or simplifying assumptions. This results in highly accurate predictions of the flow physics at an extremely high computational cost. The cost is so high due to the requirement for the grid spacing to be on the order of the Kolmogorov scale–proportional to $\mathrm{Re}^{-3/4}$. Even with the large jump in computational power in recent years, DNS is limited to research cases as it requires too much compute time for practical engineering design [8].

Richardson proposed the idea of the energy cascade, where energy is transferred from large eddies to small eddies until the eddies become small enough that dissipation due to viscous effects becomes significant. Kolmogorov hypothesized that since the large eddies are anisotropic due to the boundary conditions and geometry, some eddies are small enough that they are locally isotropic and have universal characteristics that can be modeled [30].

Smagorinsky developed the Large Eddy Simulation (LES) methodology during his study of meteorological phenomena [34]. LES introduces a spatial filter with width Δ which separates the flow variables into their resolved and unresolved components. Eddies larger than Δ are considered large eddies and eddies smaller than Δ are considered unresolved and are modeled using a sub-grid scale (SGS) model [8]. It is a powerful method that extracts the detailed turbulent flow features, although the grid and time step requirements for wall-bounded flows are computationally expensive. This trade-off has led to the development of a class of methods called hybrid RANS/LES methods.

One such method is Detached Eddy Simulation (DES) where boundary layers are treated with a RANS formulation and flow outside the boundary layer is treated with LES. This significantly reduces the computational cost compared to pure LES while retaining the ability to resolve the turbulent structures of the flow [35]. The transition between the RANS and LES formulations is done by changing the stress model at the interface, which may cause an artificial buffer layer [13]. In DES, the location of the RANS/LES interface is determined by grid resolution which may cause issues if this interface is within the boundary layer. This can cause a phenomenon known as modeled stress depletion which results in a drop in skin friction coefficient or premature separation of the boundary layer. Zonal Detached Eddy Simulation (ZDES) and Delayed Detached Eddy Simulation (DDES) have been developed to ensure that this transition occurs outside of the boundary layer and avoid the modeled stress depletion [39].

Another hybrid RANS/LES method is the Partially Averaged Navier-Stokes equations (PANS) introduced by Girimaji [12]. PANS is used to smoothly transition between RANS and DNS via the variation of the filter control parameters, which control how much turbulent kinetic energy and dissipation is being resolved versus modeled. The formulation for PANS is distinct from LES in that the flow variables are filtered according to energy content instead of length scale. In addition, the PANS formulation is identical to the unsteady RANS (URANS) equations where the model constants differ. Consequently, PANS can be quickly implemented into a CFD code with URANS capabilities [12]. Frendi and Harrison explore the benefits of a blended PANS model [9], similar to Menter's blended model, for benchmark incompressible flows. They implement the model in OpenFOAM [40] and validate it using previous PANS simulations and experimental data for wall-bounded and free shear flows.

This work extends the blended PANS (BPANS) model to the compressible regime along with its implementation in the compressible Navier-Stokes solver in the multi-physics software suite SU2 [28]. The compressible Navier-Stokes equations are filtered using a density-weighted operator introducing a generalized central moment term that must be modeled. A parametric study is conducted to analyze the effect of the ratio of resolved to modeled turbulence variables on the velocity profiles downstream of the jet.

This work is organized as follows. The governing equations are given in Chapter 2, along with a rigorous description of the filtering operator and BPANS model. The simulation conditions and the computational grid are given in Chapter 3. Qualitative and quantitative results are presented and analyzed for flow physics and compared to high-fidelity and experimental data in Chapter 4. Conclusions and future work are provided in Chapter 5.

Chapter 2. Mathematical Model

2.1 Governing Equations

The governing equations for a compressible flow are the conservation of mass, momentum, and energy

$$\frac{\partial}{\partial t}\left(\rho\right)+\frac{\partial}{\partial x_j}\left(\rho u_j\right)=0, \tag{2.1}$$

$$\frac{\partial}{\partial t}\left(\rho u_i\right)+\frac{\partial}{\partial x_j}\left(\rho u_i u_j+p\delta_{ij}\right)-\frac{\partial}{\partial x_j}\left(\sigma_{ij}\right)=0, \tag{2.2}$$

$$\frac{\partial}{\partial t}\left(\rho E\right)+\frac{\partial}{\partial x_j}\left(\left(\rho E+p\right)u_j\right)-\frac{\partial}{\partial x_j}\left(u_i\sigma_{ij}+q_j\right)=0, \tag{2.3}$$

where ρ is the density, u_i is the ith component of velocity, p is the pressure, σ_{ij} is the viscous stress tensor, q_j is the heat flux, E is the total energy defined by

$$E=e+\frac{1}{2}u_k u_k, \tag{2.4}$$

and e is the internal energy. Assuming the flow is a calorically perfect gas yields the equation of state

$$p = \rho R T, \tag{2.5}$$

and the relation of the temperature T and the internal energy e via the specific heat at constant volume c_v

$$e = c_v T. \tag{2.6}$$

The ratio of the specific heat at constant pressure c_p to c_v is defined as the ratio of specific heats γ

$$\gamma \equiv \frac{c_p}{c_v}, \tag{2.7}$$

such that the specific heats are related to the gas constant R

$$c_p - c_v = R. \tag{2.8}$$

An alternate form of the equation of state,

$$p = \rho\left(\gamma - 1\right)\left(E + \frac{1}{2}u_k u_k\right), \tag{2.9}$$

uses the above definitions and relations. The heat flux is defined using Foruier's law

$$q_j \equiv -c_p \frac{\mu}{\mathrm{Pr}} \frac{\partial T}{\partial x_j}, \tag{2.10}$$

where μ is the dynamic viscosity, Pr is the Prandtl number defined

$$\mathrm{Pr} \equiv c_p \frac{\mu}{\kappa}, \tag{2.11}$$

and κ is the thermal conductivity. The viscous stress tensor also involves μ, however, it is related to the diffusive viscous forces within the flow

$$\sigma_{ij} = 2\mu \left(S_{ij} - \frac{1}{3}\frac{\partial u_k}{\partial x_k}\delta_{ij} \right), \tag{2.12}$$

with the strain-rate tensor S_{ij}

$$S_{ij} = \frac{1}{2}\left(\frac{\partial u_i}{\partial x_j} + \frac{\partial u_j}{\partial x_i} \right). \tag{2.13}$$

2.2 Filtering Operator

We consider a filter operator $\langle \cdot \rangle$ which is linear and constant preserving,

$$\langle \Psi_1 + \Psi_2 \rangle = \langle \Psi_1 \rangle + \langle \Psi_2 \rangle, \quad \langle \alpha \Psi \rangle = \alpha \langle \Psi \rangle, \tag{2.14}$$

where Ψ is a variable and α is a constant. It also has spatial and temporal differential commutativity such that

$$\left\langle \frac{\partial \Psi}{\partial x_i} \right\rangle = \frac{\partial \langle \Psi \rangle}{\partial x_i}, \quad \left\langle \frac{\partial \Psi}{\partial t} \right\rangle = \frac{\partial \langle \Psi \rangle}{\partial t}. \tag{2.15}$$

This operator also decomposes an instantaneous flow quantity Ψ into filtered (resolved) and modeled (unresolved) components,

$$\Psi \equiv \langle \Psi \rangle + \psi, \tag{2.16}$$

where $\langle \Psi \rangle$ is the filtered component and ψ is the modeled component. This operator may be defined as a density-weighted filter,

$$\Psi \equiv \{\Psi\} + \psi^*, \tag{2.17}$$

where $\{\Psi\}$ is the density-weighted filtered component and ψ^* is the modeled fluctuating component,

$$\{\Psi\} \equiv \frac{\langle \rho \Psi \rangle}{\langle \rho \rangle}, \tag{2.18}$$

$$\psi^* = \Psi - \{\Psi\}. \tag{2.19}$$

We choose the primary variables of the filtered compressible Navier-Stokes equations to be ρ, u_i, p, and E. This choice of variables is natural given the form of the compressible Navier-Stokes equations such that u_o and E use a density-weighted filter while ρ and p use a standard filter. The use of two types of filtering operators for the primary variables indicates the need for two forms of the generalized central moment. These are defined

$$\tau^1 \left(\Psi_i, \Psi_j\right) \equiv \left\{\Psi_i \Psi_j\right\} - \left\{\Psi_i\right\} \left\{\Psi_j\right\}, \tag{2.20}$$

$$\tau^2\left(\Psi_i, \Psi_j\right) \equiv \langle \Psi_i \Psi_j \rangle - \{\Psi_i\}\langle \Psi_j \rangle, \tag{2.21}$$

such that both arguments of $\tau^1(\Psi_i, \Psi_j)$ are subject to density-weighted filters whereas the arguments of $\tau^2(\Psi_i, \Psi_j)$ are subject to density-weighted and standard filtering, respectively. These are referred to as the Favre-Filtered Generalized Central Moments (FFGCM) of the first and second kind. The FFGCMs account for the modeled turbulence within the resolved (filtered) flow field. The averaging-invariance property has been investigated by [37] where they demonstrated that the evolution equations of the FFGCM are invariant to filter width.

In the limit of all turbulence scales being modeled, these decompositions are equivalent to Reynolds-averaging and Favre-averaging,

$$\Psi = \bar{\Psi} + \psi', \tag{2.22}$$

$$\Psi = \widetilde{\Psi} + \psi'', \tag{2.23}$$

where $\bar{\Psi}$ and ψ' are the time, spatial, or ensemble-averaged and turbulent components of Ψ whereas $\widetilde{\Psi}$ and ψ'' are the density-weighted averaged and fluctuating portions of Ψ.

2.3 Filtered Compressible Navier-Stokes Equations

The application of density-weighted and standard filtering operators to the conservation of mass, momentum, and energy equations for compressible flow leads to the filtered (partially-averaged) form,

$$\frac{\partial}{\partial t}\langle\rho\rangle + \frac{\partial}{\partial x_i}\left(\langle\rho\rangle\left\{u_i\right\}\right) = 0, \tag{2.24}$$

$$\frac{\partial}{\partial t}\left(\langle\rho\rangle\left\{u_i\right\}\right) + \frac{\partial}{\partial x_j}\left(\langle\rho\rangle\left\{u_i u_j\right\} + \langle p\rangle\delta_{ij} - \ \langle\sigma_{ij}\rangle\right) = 0, \tag{2.25}$$

$$\frac{\partial}{\partial t}\left(\langle\rho\rangle\left\{E\right\}\right) + \frac{\partial}{\partial x_j}\left(\langle\rho\rangle\left\{u_j E\right\} + \langle u_j p\rangle - \langle u_i\sigma_{ij}\rangle + \langle q_j\rangle\right) = 0. \tag{2.26}$$

Here, the linear nature of the conservation of mass and the commutative properties of the filtering operator shine through as the filtering does not change its form. The same cannot be said for the conservation of momentum, where there is a closure problem due to the filtering. There is an additional term: the filtered product of u_i and u_j written as $\{u_i u_j\}$. This unclosed product is restated in terms of the product of filtered velocities $\{u_i\}\{u_j\}$ using the FFGCM of the first kind resulting in

$$\tau^1\left(u_i, u_j\right) = \left\{u_i u_j\right\} - \left\{u_i\right\}\left\{u_j\right\}. \tag{2.27}$$

Filtering the conservation of energy equation also leads to a closure problem with the additional terms $\{u_i E\}$, $\langle u_i p\rangle$, and $\langle u_i \sigma_{ij}\rangle$. Since the filters for both u_j and E are chosen as density-weighted, the first unclosed term $\{u_j E\}$ is restated in terms of the product of filtered velocity and total energy $\{u_j\}\{E\}$ using the FFGCM of the first kind

$$\tau^1\left(u_j, E\right) = \{u_j E\} - \{u_j\}\{E\}. \tag{2.28}$$

This same process is done for the unclosed terms $\{u_j p\}$ and $\{u_i \sigma_{ij}\}$, however, each term contains one variable that is subjected to standard filtering. To account for this, an FFGCM of the second kind is substituted for each term

$$\tau^2\left(u_j, p\right) = \langle u_j p\rangle - \{u_j\}\langle p\rangle, \tag{2.29}$$

$$\tau^2\left(u_i, \sigma_{ij}\right) = \langle u_i \sigma_{ij}\rangle - \{u_i\}\langle \sigma_{ij}\rangle. \tag{2.30}$$

Using these FFGCMs to substitute into the conservation of momentum and energy equations yields

$$\frac{\partial}{\partial t}\left(\langle\rho\rangle\{u_i\}\right) + \frac{\partial}{\partial x_j}\big(\langle\rho\rangle\{u_i\}\{u_j\} + \langle p\rangle\delta_{ij} - \ \langle\sigma_{ij}\rangle - \langle\rho\rangle\tau^1\left(u_i, u_j\right)\big) = 0, \tag{2.31}$$

$$\frac{\partial}{\partial t}\left(\langle\rho\rangle\left\{E\right\}\right)+\frac{\partial}{\partial x_j}\left(\langle\rho\rangle\left\{u_j\right\}\left\{E\right\}+\left\{u_j\right\}\langle p\rangle-\left\{u_i\right\}\langle\sigma_{ij}\rangle+\langle q_j\rangle\right)$$
$$+\frac{\partial}{\partial x_j}\big(\langle\rho\rangle\tau^1\left(u_j,E\right)+\tau^2\left(u_j,p\right)-\tau^2\left(u_i,\sigma_{ij}\right)\big)=0. \quad (2.32)$$

We also apply the density-weighted filtering operation to the total energy

$$\left\{E\right\}=\left\{e\right\}+\frac{1}{2}\left\{u_k u_k\right\}, \quad (2.33)$$

and an FFGCM of the first kind for the filtered product of velocities $\{u_k u_k\}$ results in the filtered total energy

$$\left\{E\right\}=\left\{e\right\}+\frac{1}{2}\left\{u_k\right\}\left\{u_k\right\}+\frac{1}{2}\tau^1\left(u_k,u_k\right). \quad (2.34)$$

In both the filtered conservation of momentum and energy equations, the viscous stress tensor is filtered such that

$$\langle\sigma_{ij}\rangle=2\mu\left(\left\{S_{ij}\right\}-\frac{2}{3}\frac{\partial}{\partial x_k}\left\{u_k\right\}\delta_{ij}\right), \quad (2.35)$$

where $\{S_{ij}\}$ is the filtered strain rate tensor

$$\left\{S_{ij}\right\}=\frac{1}{2}\left(\frac{\partial}{\partial x_j}\left\{u_i\right\}+\frac{\partial}{\partial x_i}\left\{u_j\right\}\right). \quad (2.36)$$

The choice of S_{ij} to be subjected to density-weighted filtering is natural due to its definition being a function of velocity gradients. The heat flux is subjected to a standard filter

$$\langle q_j \rangle = -c_p \frac{\mu}{\mathrm{Pr}} \frac{\partial}{\partial x_j} \langle T \rangle \tag{2.37}$$

and a similar procedure is conducted for the equation of state resulting in its filtered form

$$\langle p \rangle = \langle \rho \rangle (\gamma - 1) \left(\{E\} - \frac{1}{2} \{u_k u_k\} \right), \tag{2.38}$$

and substituting the unfiltered velocity times itself with the FFGCM of the first kind yields

$$\langle p \rangle = \langle \rho \rangle (\gamma - 1) \left(\{E\} - \frac{1}{2} \{u_k\} \{u_k\} - \frac{1}{2} \tau^1 (u_k, u_k) \right), \tag{2.39}$$

where the unresolved turbulent kinetic energy k_u is defined as

$$k_u = \frac{1}{2} \tau^1 (u_k, u_k) . \tag{2.40}$$

For thoroughness, the equation of state with k_u is given

$$\langle p \rangle = \langle \rho \rangle (\gamma - 1) \left(\{E\} - \frac{1}{2} \{u_k\} \{u_k\} - k_u \right). \tag{2.41}$$

2.4 Constitutive Relationships

Multiple FFGCMs are unclosed within the filtered compressible Navier-Stokes equations and must be modeled to ensure closure of the system of equations. This is accomplished for the $\tau^1 (u_i, u_j)$ term using the Boussinesq approximation [33], which establishes a relationship between the transfer of momentum from the molecular gas and turbulent motion

$$\tau^1 (u_i, u_j) \equiv 2 \frac{\mu_t}{\langle\rho\rangle} \left(\{S_{ij}\} - \frac{1}{3} \frac{\partial}{\partial x_k} \{u_k\} \right) - \frac{2}{3} k_u \delta_{ij}. \tag{2.42}$$

The turbulent viscosity μ_t is commonly referred to as the eddy viscosity and represents the dissipative viscosity of the unresolved (modeled) eddies. The following constitutive relationship

$$\langle\rho\rangle \tau^1 (u_j, E) + \tau^2 (u_j, p) \equiv c_p \frac{\mu_t}{\mathrm{Pr}_t} \frac{\partial}{\partial x_j} \langle T \rangle + \langle\rho\rangle \{u_i\} \tau^1 (u_i, u_j) \tag{2.43}$$

results from an expansion of the total energy and pressure terms and a gradient approximation for the turbulent correlation between the velocity and temperature. The first term is is interpreted as the turbulent heat flux, hence the use of μ_t and the turbulent Prandtl number Pr_t. It is important to note that the second term involves an FFGCM, however, the constitutive relation for this term has been discussed above and is not addressed further.

The term $\tau^2\left(u_i, \sigma_{ij}\right)$ is interpreted as the interaction of the turbulent kinetic energy and the viscosity of the unresolved scales, thus it is natural to approximate using a gradient expression of the form

$$\tau^2\left(u_i, \sigma_{ij}\right) \approx \left(\mu + \sigma^* \mu_t\right) \frac{\partial k_u}{\partial x_j}, \tag{2.44}$$

where σ^* is a coefficient. It is argued, however, that this term may be neglected if the turbulent kinetic energy is small compared to the filtered enthalpy

$$k_u << \langle h \rangle, \tag{2.45}$$

where the enthalpy h is related to temperature via $h = c_p T$. This holds true for most flows below the hypersonic regime, which is considered in this work, thus the term is neglected. The resulting filtered compressible Navier-Stokes equations with the defined constitutive relations are given

$$\begin{aligned}\frac{\partial}{\partial t}\left(\langle\rho\rangle\left\{u_i\right\}\right) + \frac{\partial}{\partial x_j}\left(\langle\rho\rangle\left\{u_i\right\}\left\{u_j\right\} + \langle p\rangle\delta_{ij} - \langle\sigma_{ij}\rangle\right)& \\ - \frac{\partial}{\partial x_j}\left(2\mu_t\left(\left\{S_{ij}\right\} - \frac{1}{3}\frac{\partial}{\partial x_k}\left\{u_k\right\}\right) - \frac{2}{3}k_u\delta_{ij}\right) &= 0, \end{aligned} \tag{2.46}$$

$$\frac{\partial}{\partial t}\left(\langle\rho\rangle\{E\}\right)+\frac{\partial}{\partial x_j}\left(\langle\rho\rangle\{u_j\}\{E\}+\{u_j\}\langle p\rangle+\langle q_j\rangle+\langle q_j^*\rangle\rangle\right)$$
$$-\frac{\partial}{\partial x_j}\left(\{u_i\}\langle\sigma_{ij}\rangle+2\mu_t\left(\{S_{ij}\}-\frac{1}{3}\frac{\partial}{\partial x_k}\{u_k\}\right)-\frac{2}{3}k_u\delta_{ij}\right)=0, \quad (2.47)$$

where q_j^* is the turbulent heat flux

$$\langle q_j^*\rangle \equiv -c_p\frac{\mu_t}{\mathrm{Pr}_t}\frac{\partial}{\partial x_j}\langle T\rangle. \quad (2.48)$$

These equations may be simplified further using the definitions of the viscous stress tensor and heat fluxes such that

$$\frac{\partial}{\partial t}\left(\langle\rho\rangle\{u_i\}\right)+\frac{\partial}{\partial x_j}\left(\langle\rho\rangle\{u_i\}\{u_j\}+\langle p\rangle\delta_{ij}\right)$$
$$-\frac{\partial}{\partial x_j}\left(2\left(\mu+\mu_t\right)\left(\{S_{ij}\}-\frac{1}{3}\frac{\partial}{\partial x_k}\{u_k\}\right)-\frac{2}{3}k_u\delta_{ij}\right)=0, \quad (2.49)$$

$$\frac{\partial}{\partial t}\left(\langle\rho\rangle\{E\}\right)+\frac{\partial}{\partial x_j}\left(\langle\rho\rangle\{u_j\}\{E\}+\{u_j\}\langle p\rangle-c_p\left(\frac{\mu}{\mathrm{Pr}}+\frac{\mu_t}{\mathrm{Pr}_t}\right)\frac{\partial}{\partial x_j}\langle T\rangle\right)$$
$$-\frac{\partial}{\partial x_j}\left(\{u_i\}\langle\sigma_{ij}\rangle+2\left(\mu+\mu_t\right)\left(\{S_{ij}\}-\frac{1}{3}\frac{\partial}{\partial x_k}\{u_k\}\right)-\frac{2}{3}k_u\delta_{ij}\right)=0. \quad (2.50)$$

The conservation of energy equation still contains a term with the temperature, which can be simplified using the filtered equation of state to attain a form with the filtered pressure and density

$$\frac{\partial}{\partial t}\left(\langle\rho\rangle\{E\}\right)+\frac{\partial}{\partial x_j}\left(\langle\rho\rangle\{u_j\}\{E\}+\{u_j\}\langle p\rangle-\frac{\gamma}{\gamma-1}\left(\frac{\mu}{\mathrm{Pr}}+\frac{\mu_t}{\mathrm{Pr}_t}\right)\frac{\partial}{\partial x_j}\left(\frac{\langle p\rangle}{\langle\rho\rangle}\right)\right)$$
$$-\frac{\partial}{\partial x_j}\left(2\{u_i\}(\mu+\mu_t)\left(\{S_{ij}\}-\frac{1}{3}\frac{\partial}{\partial x_k}\{u_k\}\right)-\frac{2}{3}k_u\delta_{ij}\right)=0. \quad (2.51)$$

In the limit of all turbulence being modeled, the filtered compressible Navier Stokes equations are exactly equivalent to the Favre-Averaged Navier-Stokes equations

$$\frac{\partial}{\partial t}\left(\bar{\rho}\right)+\frac{\partial}{\partial x_j}\left(\bar{\rho}\widetilde{u}_j\right)=0, \quad (2.52)$$

$$\frac{\partial}{\partial t}\left(\bar{\rho}\widetilde{u}_i\right)+\frac{\partial}{\partial x_j}\left(\bar{\rho}\widetilde{u}_i\widetilde{u}_j+\bar{p}\delta_{ij}-\bar{\sigma}_{ij}\right)=0, \quad (2.53)$$

$$\frac{\partial}{\partial t}\left(\bar{\rho}\widetilde{E}\right)+\frac{\partial}{\partial x_j}\left(\bar{\rho}\widetilde{u}_j\widetilde{E}+\widetilde{u}_j\bar{p}+\bar{q}_j+\bar{q}_j^*-\widetilde{u}_k\bar{\sigma}_{kj}\right)=0, \quad (2.54)$$

with the appropriate equation of state.

2.5 Filter Control Parameter

In classical Large Eddy Simulation (LES), the resolution of the resolved scales is inversely proportional to the grid size. Thus, the physical resolution is closely coupled to the resolution of the numerical methods. In PANS, and analogously RANS, the closure model is decoupled from the numerical resolution and in the case of PANS is directly related to the filter control parameters. These parameters f_k and f_ϵ must be specified for each simulation depending on the desired physical resolution and computational cost associated with it.

In PANS modeling, it is paramount to have knowledge of the turbulent kinetic energy and turbulent dissipation a-priori to determine the length, velocity, and time scales of the largest unresolved scales, as well as the same scales for the unresolved dissipative motion [29]. In these relations, the ratio of unresolved to resolved turbulent kinetic energy and turbulent dissipation are defined as

$$f_k \equiv \frac{k_u}{k}, \tag{2.55}$$

$$f_\epsilon \equiv \frac{\epsilon_u}{\epsilon}, \tag{2.56}$$

which are used to quantify the extent of PANS filtering. f_k and f_ϵ are the partial-average quantification and, thus, referred to as the filter control parameters. The turbulent physics dictate that the large scales contain most of the kinetic energy and most of the dissipation occurs in the smallest scales, dictating the inequality $0 \leq f_k \leq f_\epsilon \leq 1$. This corresponds to DNS when $f_k = 0$ and RANS when $f_k = 1$.

A value of 1 for f_ϵ implies that the unresolved scales of PANS and RANS are identical, thus smaller values of f_ϵ require the resolution of the dissipative scales. It may be desirable to vary the values of the filter control parameters through space and time, however, in this work, their variation is assumed to be smaller than that of the flow variables and are assumed constant.

2.6 PANS Model Development

The goal is now to develop a model that accurately reflects the physics characterized by scales smaller than the filter width. The averaging invariance principle [37] allows the use of LES or RANS-like closure models. Some of the most popular LES closure models are algebraic, dubbed zero-equation models, and are best suited for wave number cutoffs in the small inertial scales of motion. RANS models, however, are developed with averaging over all scales of motion and thus contain sufficient physics to represent the partially-averaged fields. Given the purpose of PANS being used at all degrees of resolution ranging from RANS to DNS, it is argued that there must be at least as much physics as in some of the two-equation RANS models. Therefore, the PANS models used in this work are based on the RANS two-equation models.

A few commonly used RANS models are the $(k-\epsilon)$ [41] and $(k-\omega)$ [17] models which are great at handling free shear and wall-bounded flows, respectively. The $(k-\omega)$ SST [22] model was derived as a blending between the two models to make use of each of their strengths. This blending function is directly dependent on the wall distance, holding values between zero and one to represent which form the model takes at that point in the spatial domain. Effectively, the SST model takes a $(k - \omega)$ form when near the wall and a $(k - \epsilon)$ form when far away from the wall. These two-equation models solve for two turbulence variables, namely the turbulent kinetic energy k and either the specific dissipation rate ω or turbulent dissipation ϵ. These models all take advantage of the concept of the eddy viscosity, which is defined as

$$\mu_t = \bar{\rho}\frac{k_u}{\omega_u}, \tag{2.57}$$

for a $(k - \omega)$ model. This is the definition used in this work, though it is common to use the magnitude of the strain or vorticity tensors in a limiting sense when calculating the eddy viscosity. The idea of blending two models similar to the SST model is taken into the PANS framework. We start with the $(k - \epsilon)$ PANS model from [12]

$$\frac{\partial}{\partial x_j}\left(\bar{\rho} k_u\right) + \frac{\partial}{\partial x_j}\left(\bar{\rho}\widetilde{u}_j k_u\right) = P - \bar{\rho}\epsilon_u + \frac{\partial}{\partial x_j}\left(\left(\mu + \sigma_{k2}\mu_t\right)\frac{\partial k_u}{\partial x_j}\right), \tag{2.58}$$

$$\frac{\partial}{\partial t}\left(\bar{\rho}\epsilon_u\right) + \frac{\partial}{\partial x_j}\left(\bar{\rho}\widetilde{u}_j \epsilon_u\right) = C_{\epsilon 1} P \frac{\epsilon_u}{k_u} - C^*_{\epsilon 2}\bar{\rho}\frac{\epsilon_u^2}{k_u} + \frac{\partial}{\partial x_j}\left(\left(\mu + \sigma_{\epsilon}\mu_t\right)\frac{\partial \epsilon_u}{\partial x_j}\right), \tag{2.59}$$

where ϵ_u is the turbulence dissipation rate. The production terms P are evaluated via

$$P = \tau^1(u_i, u_j)\frac{\partial \widetilde{u_i}}{\partial x_j}, \tag{2.60}$$

where the constitutive relation 4.2 is used for the FFGCM. In this PANS form, there are the coefficients $C^*_{\epsilon 2}$, σ_ϵ, and σ_{k2}

$$C^*_{\epsilon 2} \equiv C_{\epsilon 1} + \frac{f_k}{f_\epsilon}\left(C_{\epsilon 2} - C_{\epsilon 1}\right), \tag{2.61}$$

$$\sigma_\epsilon \equiv \frac{1}{\sigma_{\epsilon R}}\frac{f_\epsilon}{f_k^2}, \tag{2.62}$$

$$\sigma_{k2} \equiv \frac{1}{\sigma_{kR}}\frac{f_\epsilon}{f_k^2}, \tag{2.63}$$

which are defined as functions of the filter control parameters f_k and f_ϵ. The other constants have values of $C_{\epsilon 1} = 1.42$, $C_{\epsilon 2} = 1.92$, $\sigma_{kR} = 1.0$, and $\sigma_{\epsilon R} = 1.3$ where the subscript R refers to the coefficient from the corresponding RANS model. The ϵ_u equation is rewritten in a form with the specific turbulent frequency ω_u using the relation

$$\epsilon_u = \beta^* k_u \omega_u. \tag{2.64}$$

This leaves the temporal and convective terms in the following form

$$\frac{\partial}{\partial t}\left(\bar{\rho}\epsilon_u\right) = \beta^*\left(k_u\frac{\partial}{\partial t}\left(\bar{\rho}\omega_u\right) + \omega_u\frac{\partial}{\partial t}\left(\bar{\rho}k_u\right)\right), \tag{2.65}$$

$$\frac{\partial}{\partial x_j}\left(\bar{\rho}\widetilde{u_j}\epsilon_u\right) = \beta^*\left(k_u\frac{\partial}{\partial t}\left(\bar{\rho}u_j\omega_u\right) + \omega_u\frac{\partial}{\partial t}\left(\bar{\rho}u_jk_u\right)\right), \tag{2.66}$$

and a similar procedure for the production terms yields

$$C_{\epsilon 1}P\frac{\epsilon_u}{k_u} = C_{\epsilon 1}P\beta^*\omega_u, \tag{2.67}$$

$$C^*_{\epsilon 2}\bar{\rho}\frac{\epsilon_u^2}{k_u} = C^*_{\epsilon 2}\bar{\rho}\beta^*k_u\omega_u^2. \tag{2.68}$$

The viscous term has a slightly more complex form due to the gradient terms, but nonetheless is treated the same as above

$$\begin{aligned}\frac{\partial}{\partial x_j}\left(\left(\mu+\sigma_\epsilon\mu_t\right)\frac{\partial\epsilon_u}{\partial x_j}\right) &= \beta^*k_u\frac{\partial}{\partial x_j}\left(\left(\mu+\sigma_\epsilon\mu_t\right)\frac{\partial\omega_u}{\partial x_j}\right)\\ &+ \beta^*\omega_u\frac{\partial}{\partial x_j}\left(\left(\mu+\sigma_\epsilon\mu_t\right)\frac{\partial k_u}{\partial x_j}\right) + 2\beta^*\left(\mu+\sigma_\epsilon\mu_t\right)\frac{\partial k_u}{\partial x_j}\frac{\partial\omega_u}{\partial x_j},\end{aligned} \tag{2.69}$$

where it is important to note the extra cross-diffusion term. This extra term is key to the form of the blended model, which will be seen shortly. Substituting this all back into the original equation and doing some rearranging results in

$$\begin{aligned}\beta^*\omega_u\left[\frac{\partial}{\partial x_j}\left(\bar{\rho}k_u\right)+\frac{\partial}{\partial x_j}\left(\bar{\rho}\widetilde{u}_jk_u\right)-P+\beta^*\bar{\rho}k_u\omega_u-\frac{\partial}{\partial x_j}\left(\left(\mu+\sigma_{k2}\mu_t\right)\frac{\partial k_u}{\partial x_j}\right)\right]&\\+\beta^*k_u\left[\frac{\partial}{\partial t}\left(\bar{\rho}\omega_u\right)+\frac{\partial}{\partial x_j}\left(\bar{\rho}\widetilde{u}_j\omega_u\right)\right]=(C_{\epsilon1}-1)P\beta^*\omega_u-(C^*_{\epsilon2}-1)\bar{\rho}\beta^{*2}k_u\omega_u^2&\\+\beta^*k_u\frac{\partial}{\partial x_j}\left(\left(\mu+\sigma_\epsilon\mu_t\right)\frac{\partial\omega_u}{\partial x_j}\right)+2\beta^*\left(\mu+\sigma_\epsilon\mu_t\right)\frac{\partial k_u}{\partial x_j}\frac{\partial\omega_u}{\partial x_j}.&\quad(2.70)\end{aligned}$$

Since the first bracketed term is the original k_u equation it can be taken as zero, which simplifies the transformed equation to

$$\begin{aligned}\frac{\partial}{\partial t}\left(\bar{\rho}\omega_u\right)+\frac{\partial}{\partial x_j}\left(\bar{\rho}\widetilde{u}_j\omega_u\right)=(C_{\epsilon1}-1)P\frac{\omega_u}{k_u}-(C^*_{\epsilon2}-1)\bar{\rho}\beta^*\omega_u^2&\\+\frac{\partial}{\partial x_j}\left(\left(\mu+\sigma_\epsilon\mu_t\right)\frac{\partial\omega_u}{\partial x_j}\right)+\frac{2}{k_u}\left(\mu+\sigma_\epsilon\mu_t\right)\frac{\partial k_u}{\partial x_j}\frac{\partial\omega_u}{\partial x_j},&\quad(2.71)\end{aligned}$$

where the cross-diffusion term has both the dynamic and turbulent viscosity. According to [23], the dynamic viscosity can be neglected in the cross-diffusion term which yields

$$\begin{aligned}\frac{\partial}{\partial t}\left(\bar{\rho}\omega_u\right)+\frac{\partial}{\partial x_j}\left(\bar{\rho}\widetilde{u}_j\omega_u\right)=(C_{\epsilon1}-1)P\frac{\omega_u}{k_u}-(C^*_{\epsilon2}-1)\bar{\rho}\beta^*\omega_u^2&\\+\frac{\partial}{\partial x_j}\left(\left(\mu+\sigma_\epsilon\mu_t\right)\frac{\partial\omega_u}{\partial x_j}\right)+2\frac{\bar{\rho}\sigma_\epsilon}{\omega_u}\frac{\partial k_u}{\partial x_j}\frac{\partial\omega_u}{\partial x_j},&\quad(2.72)\end{aligned}$$

by substituting the relation for the eddy viscosity 4.2. The coefficients of the production terms are redefined as the model coefficients

$$\gamma_2 \equiv C_{\epsilon 1} - 1, \tag{2.73}$$

$$\beta_2 \equiv \beta^* \left(C^*_{\epsilon 2} - 1\right), \tag{2.74}$$

which when substituted into the transformed ϵ_u equation yields the ω_u equation

$$\begin{aligned}\frac{\partial}{\partial t}\left(\bar{\rho}\omega_u\right) + \frac{\partial}{\partial x_j}\left(\bar{\rho}\widetilde{u}_j\omega_u\right) = \gamma_2 P\frac{\omega_u}{k_u} - \beta_2\bar{\rho}\omega_u^2 \\ + \frac{\partial}{\partial x_j}\left(\left(\mu + \sigma_\epsilon \mu_t\right)\frac{\partial \omega_u}{\partial x_j}\right) + 2\frac{\bar{\rho}\sigma_{\omega 2}}{\omega_u}\frac{\partial k_u}{\partial x_j}\frac{\partial \omega_u}{\partial x_j}.\end{aligned} \tag{2.75}$$

The $(k - \omega)$ PANS model [19] is given as

$$\frac{\partial}{\partial x_j}\left(\bar{\rho}k_u\right) + \frac{\partial}{\partial x_j}\left(\bar{\rho}\widetilde{u}_j k_u\right) = P - \beta^*\bar{\rho}k_u\omega_u + \frac{\partial}{\partial x_j}\left(\left(\mu + \sigma_{k1}\mu_t\right)\frac{\partial k_u}{\partial x_j}\right), \tag{2.76}$$

$$\frac{\partial}{\partial t}\left(\bar{\rho}\omega_u\right) + \frac{\partial}{\partial x_j}\left(\bar{\rho}\widetilde{u}_j\omega_u\right) = \gamma_1 P\frac{\omega_u}{k_u} - \beta_1\bar{\rho}\omega_u^2 + \frac{\partial}{\partial x_j}\left(\left(\mu + \sigma_{\omega 1}\mu_t\right)\frac{\partial \omega_u}{\partial x_j}\right), \tag{2.77}$$

where the model coefficients are defined

$$\gamma_1 \equiv \alpha, \tag{2.78}$$

$$\beta_1 \equiv \alpha\beta^* \left(1 - \frac{f_k}{f_\epsilon}\right) + \beta\frac{f_k}{f_\epsilon}, \tag{2.79}$$

$$\sigma_{k1} \equiv \frac{1}{\sigma_{kR}}, \tag{2.80}$$

$$\sigma_{\omega 1} \equiv \frac{1}{\sigma_{\omega R}}\frac{f_\epsilon}{f_k^2}. \tag{2.81}$$

There are several constants used to calculate these coefficients, including $\alpha = 5/9$, $\beta^* = 0.09$, $\sigma_{kR} = 2.0$, and $\sigma_{\omega R} = 2.0$. Finally, the $(k - \epsilon)$ PANS transformed into ω_u form and the $(k - \omega)$ PANS are bridged together into the Blended PANS (BPANS) model. This is done by defining a blending function F

$$F = \tanh arg^4, \tag{2.82}$$

$$arg = \min\left(\max\left(\frac{\sqrt{k_u}}{\beta^*\omega_u y}, \frac{500\mu}{\bar{\rho}\omega_u y^2}\right), \frac{4\bar{\rho}\sigma_{\omega 2}k_u}{\mathrm{CD}_{k\omega}y^2}\right), \tag{2.83}$$

$$\mathrm{CD}_{k\omega} = \max\left(2\frac{\bar{\rho}\sigma_{\omega 2}}{\omega_u}\frac{\partial k_u}{\partial x_j}\frac{\partial \omega_u}{\partial x_j}, 10^{-20}\right), \tag{2.84}$$

where $\mathrm{CD}_{k\omega}$ is the cross-diffusion between the two turbulence fields and y is the distance to the nearest wall. This function is used to blend the coefficients of each model such that

$$\psi = F\psi_1 + (1 - F)\psi_2, \tag{2.85}$$

where each ψ represents the corresponding coefficient from each model. The blending is done by multiplying the $(k - \omega)$ PANS equations by F and the transformed $(k - \epsilon)$ PANS equations by $(1 - F)$,

$$\frac{\partial}{\partial x_j}\left(\bar{\rho} k_u\right) + \frac{\partial}{\partial x_j}\left(\bar{\rho}\widetilde{u_j} k_u\right) = P - \beta^* \bar{\rho} k_u \omega_u + \frac{\partial}{\partial x_j}\left(\left(\mu + \sigma_k \mu_t\right)\frac{\partial k_u}{\partial x_j}\right), \tag{2.86}$$

$$\begin{aligned}\frac{\partial}{\partial t}\left(\bar{\rho}\omega_u\right) + \frac{\partial}{\partial x_j}\left(\bar{\rho}\widetilde{u_j}\omega_u\right) = \gamma P \frac{\omega_u}{k_u} - \beta \bar{\rho}\omega_u^2 \\ + \frac{\partial}{\partial x_j}\left(\left(\mu + \sigma_\epsilon \mu_t\right)\frac{\partial \omega_u}{\partial x_j}\right) + 2\left(1 - F\right)\frac{\bar{\rho}\sigma_\omega}{\omega_u}\frac{\partial k_u}{\partial x_j}\frac{\partial \omega_u}{\partial x_j}.\end{aligned} \tag{2.87}$$

This is the final BPANS model, where the model coefficients γ, β, σ_k, and σ_ω are blended coefficients. Upon inspection, the form of the BPANS equations is the same as the SST model with different values for the model coefficients. In BPANS, they are directly dependent on the values of the filter control parameters and thus the coefficients must be recalculated prior to a new simulation. This is useful, as this model can be implemented into a CFD software that already has the SST model quite easily [12]—it is only a change of coefficients.

Chapter 3. Numerical Model

The open-source multi-physics software Stanford University Unstructured (SU2) [28] is used to setup and solve the numerical model. SU2 is a finite volume based solver that utilizes a standard edge-based data structure on a dual grid with vertex-based schemes. The convective and viscous fluxes are evaluated at the midpoint of an edge. SU2 is developed and maintained by a group of dedicated individuals from the SU2 Foundation, along with many other contributors on their Github. There is a large suite of methods available to solve complex multi-physics problems and the ones used are discussed here.

For viscous, compressible flow, SU2 solves the Favre-Averaged Navier-Stokes (FANS) equations given in Eq. 2.52, 2.53, and 2.54. The equations are implemented in a density-based solver in residual form

$$R(\bar{V}) = \frac{\partial \bar{V}}{\partial t} + \nabla \cdot \bar{F}^c(\bar{V}) - \nabla \cdot \bar{F}^v(\bar{V}, \nabla \bar{V}) - \bar{Q} = 0, \tag{3.1}$$

where $\bar{V}$ are the conservative variables, $\nabla \cdot \bar{F}^c(\bar{V})$ are the convective fluxes, and $\nabla \cdot \bar{F}^c(\bar{V}, \nabla \bar{V})$ are the viscous fluxes. The conservative variables

$$\bar{V} = \left\{ \begin{matrix} \bar{\rho} \\ \bar{\rho}\widetilde{u}_i \\ \bar{\rho}\widetilde{E} \end{matrix} \right\}, \tag{3.2}$$

are the working variables of the solver, while the convective and viscous fluxes are given as

$$\bar{F}^c(V) = \left\{ \begin{matrix} \bar{\rho}\widetilde{u}_i \\ \bar{\rho}\widetilde{u}_i\widetilde{u}_j + \bar{p}\delta_{ij} \\ \bar{\rho}\widetilde{u}_j\widetilde{E} + \bar{p}\widetilde{u}_j \end{matrix} \right\}, \tag{3.3}$$

$$\bar{F}^v(V, \nabla V) = \left\{ \begin{matrix} . \\ \bar{\sigma}_{ij} \\ \widetilde{u}_k\bar{\sigma}_{kj} + \bar{q}_j + \bar{q}_j^* \end{matrix} \right\}, \tag{3.4}$$

and $\bar{Q}$ is the source term vector. The convective fluxes are discretized using the JST [16] central scheme with 0.5 and 0.0 as the second and fourth-order dissipation coefficients, respectively. The gradients are reconstructed using a nodal Green-Gauss method and the BPANS model is discretized using an upwind method.

3.1 Simulation Setup

The freestream conditions are set given the crossflow Mach number and Reynolds number based on the jet diameter

$$\mathrm{Re}_D = \frac{\rho_\infty U_\infty D}{\mu_\infty}, \tag{3.5}$$

where ρ_∞ is the freestream density, U_∞ is the freestream velocity, μ_∞ is the freestream viscosity, and D is the diameter of the jet exit. The target Reynolds number is $\mathrm{Re}_D = 5.9 \times 10^4$ and the free stream Mach number is 1.6. The ratio of densities between the nozzle chamber and the crossflow is $\rho_{0j}/\rho_\infty = 5.5$ and the ratio of pressures between the nozzle chamber and the crossflow is $p_{0j}/p_\infty = 8.4$. This results in a jet-to-crossflow momentum flux ratio

$$J = \frac{\rho_j U_j^2}{\rho_\infty U_\infty^2} = \frac{\gamma_j p_j M_j^2}{\gamma_\infty p_\infty M_\infty^2} \tag{3.6}$$

of 1.7. The diameter of the jet exit is 4 millimeters. The stagnation pressure of the jet p_{0j} is 476 kpa, the stagnation temperature of the jet is T_{0j} is 295 K, and the freestream velocity U_∞ is given as 446 m/s. These conditions result in the freestream viscosity $\mu_\infty = 3.09086 \times 10^{-5}\ kg/(m\ s)$, where the viscosity is a function of temperature according to Sutherland's law [38], the freestream temperature $T_\infty = 193.1548\ K$. The Sutherland coefficient is set to $S = 110.4$, the reference viscosity and temperature are set to the respective freestream conditions $\mu_{ref} = \mu_\infty$ and $T_{ref} = T_\infty$. The domain is assumed to only have air, which has a ratio of specific heats $\gamma = 1.4$, a gas constant $R = 287.058\ J/(kg\ K)$, laminar Prandtl number $\mathrm{Pr} = 0.72$, and turbulent Prandtl number $\mathrm{Pr}_t = 0.90$.

It is important to note that the Reynolds number for the experimental data used in Chapter 4 is $\mathrm{Re}_D = 2.4 \times 10^5$, which is four times the Reynolds number of the problem setup in this work. This is done due to the computational cost of setting up high Reynolds number LES. Kawai and Lele [18] used a Reynolds number 1/10 of the experimental data and still obtained reasonable agreement of the mean quantities, thus it is assumed that reducing the Reynolds number should not affect the flow structures and mean quantities of the jet in crossflow.

At the inlet of the jet, the total conditions and direction of the velocity vector are specified using a total inlet boundary condition. The total pressure and temperature are specified as 476 kPa and 295 K to match the jet exit conditions from the experimental data. The crossflow is assigned a supersonic inlet boundary condition with a constant velocity profile of 446 m/s and a total pressure and temperature of 56.667 kPa and 193.155 K. The bottom wall surrounding the jet exit and the walls of the jet are treated as no-slip walls with zero heat flux. The outlet is set as a pressure outlet with a static pressure of 1 Pa, since setting it to 0 Pa crashes the solver. The top of the domain is set to a freestream condition and the sides are assigned periodic boundary conditions.

Dual time stepping is the temporal scheme used for the unsteady flow, with an implicit Euler scheme for the five sub-iterations. An implicit Euler scheme is also used for the BPANS model. The unsteady simulations are initialized using a steady solution with the SST model. Starting from this solution, an unsteady simulation is run until the transient phenomena have settled into a statistically-steady state. Once that state is reached, the BPANS model is turned on and run with the scheme and time step previously specified. The time step used is $\Delta t = 5.575 D/U_\infty$, and is advanced for 1000 time steps. The unsteady results are averaged over all 1000 time steps to conduct an analysis of the averaged flow statistics.

3.2 Computational Mesh

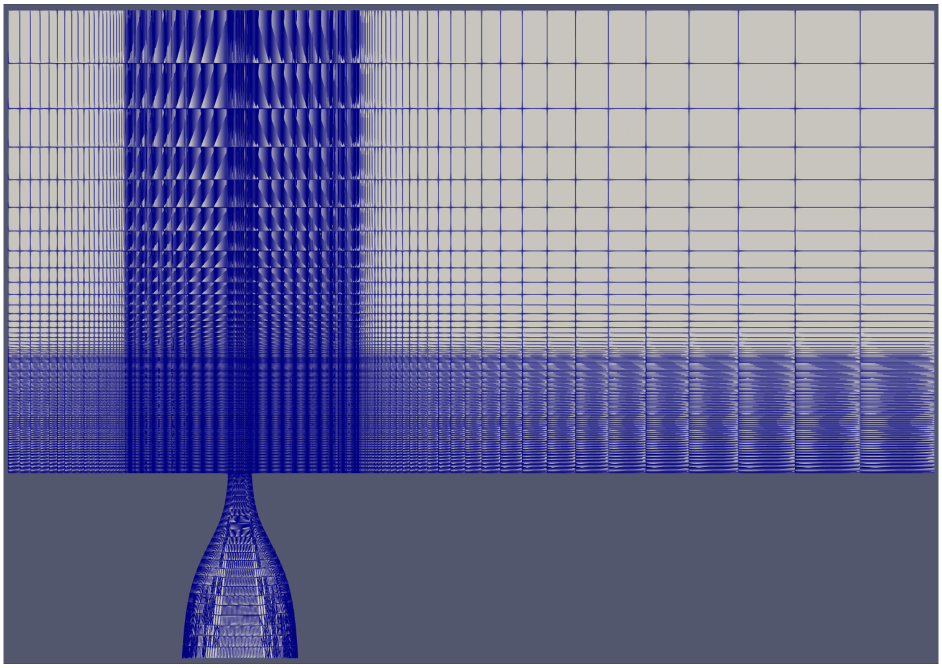

Figure 3.1: Central plane of grid for numerical simulations.

The computational mesh and domain for the numerical simulation of the high speed JICF problem is shown in Figure 3.1. The origin of the coordinates is set at the center of the jet exit, with the domain spanning $40D$, $20D$, and $30D$ in the streamwise, wall-normal, and spanwise directions, respectively. These also correspond to the x, y, and z directions in the domain. In [5] they claim that preliminary computations show that the domain is large enough such that the confinement effect of the boundaries is not seen in the flow.

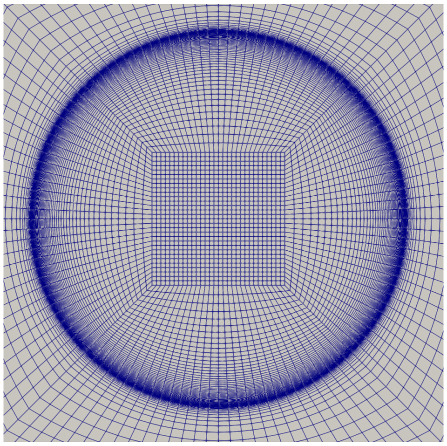

Figure 3.2: Grid refinement inside the jet nozzle.

blockMesh [40] is used to generate multi-block, structured grids which are converted to work with SU2. This is done by reading in the points, faces, neighbor, and boundary files output by blockMesh, then building the cells and their connectivity. Since SU2 is an unstructured solver, the order of the points and cells, as well as their connectivity and the boundary markers, is irrelevant. The points, cells, connectivity, and boundary markers are then output in the specific format that is readable by SU2. It is important to note that SU2 has a unique file format that no other software uses. gmsh [11] is an open-source meshing software that does have the capability to output in the SU2 format, however, a structured mesh was desired so the mesh conversion process from blockMesh was approached instead.

The grid has a total of approximately 6.5 million hexahedral cells. It is refined within the critical regions of the flow, such as the surface of the flat plate, the wall of the jet nozzle, and the field near the jet stream. The streamwise spacing just downstream of the jet is set to $\Delta x \approx 0.03D$ to ensure a fine enough

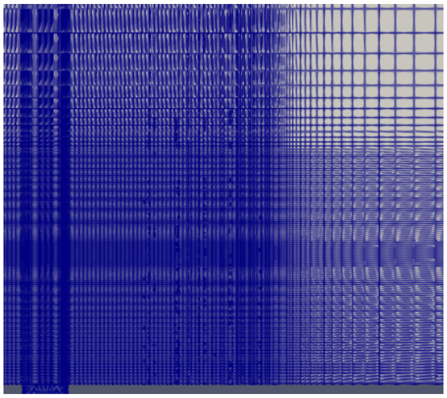

Figure 3.3: Refined area of grid near the jet exit.

resolution to analyze the flow structures and is stretched towards the outlet. The boundary layer on the flat plate is resolved using a stretched layer with 20 cells with a first cell thickness of $0.000025D$. A similar stretched layer is used for the walls of the jet, with the same first cell thickness and 15 cells instead of 20. These stretched layers achieve the target nondimensionalized wall distance y^+ on the order of one, and there are a few points within the viscous sublayer ($y^+ \leq 5$) to capture the boundary layer profile. Outside of the boundary layer, the wall-normal cell spacing is set to $\Delta y \approx 0.03D$ and is stretched towards the freestream. The spanwise spacing is dictated by the angular spacing of cells within jet nozzle, which is also set to $\Delta z \approx 0.03D$. The cell spacing in all directions near the jet exit outside of the boundary layer results in low aspect ratio cells. Within the jet nozzle, an O-grid is used to achieve the circular geometry with a stretched layer near the walls, as previously mentioned, and stretched cells near the center of the nozzle. Zoomed-in views of the grid in both the jet nozzle and the region near the jet exit are provided in Figure 3.2 and 3.3, respectively.

3.3 Filter Control Parameter Estimation

The filter control parameter f_k is estimated a-priori to ensure that the computational mesh can resolve the scales dictated by f_k. This is done using the relation

$$f_k \geq \left(\frac{\Delta}{L_t} \right)^{\frac{2}{3}}, \tag{3.7}$$

where Δ is the local grid sizing defined as the cube root of the cell volume and L_t is the local turbulent length scale defined as $L_t \equiv \frac{\sqrt{k_u}}{\beta^* \omega_u}$. The values of f_k are manually inspected in the regions of interest to determine if the grid resolution is fine enough for the desired f_k value of 0.2. The simulations are run on increasingly refined grids until the current iteration, which resolves the JICF case with $f_k =$ 0.2.

Chapter 4. Results and Discussion

4.1 Flow Physics

The highly unsteady JICF produces many types of structures that construct the flow physics of this problem. The Q-criterion [15] is used to visualize these structures and is defined as the second invariant of the velocity gradient tensor

$$Q = \frac{1}{2}\left[\left(\frac{\partial \widetilde{u}_i}{\partial x_i}\right)^2 - \frac{\partial \widetilde{u}_i}{\partial x_j}\frac{\partial \widetilde{u}_j}{\partial x_i}\right], \tag{4.1}$$

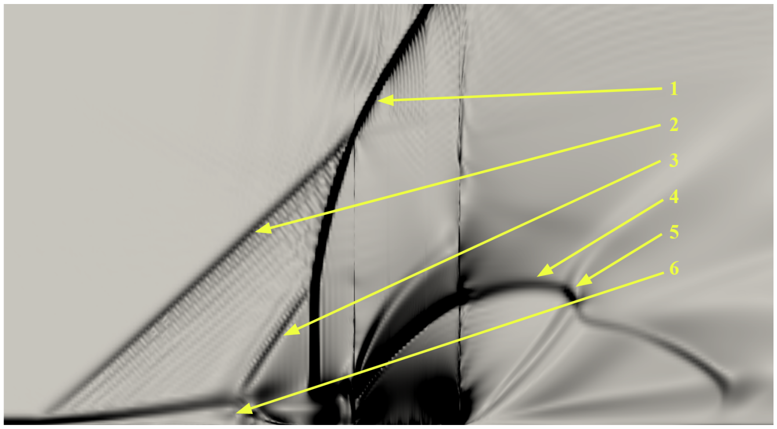

Figure 4.1: Numerical schlieren on the central plane ($z/D = 0$) showing the different shock structures: 1. bow shock, 2. weak lambda shock, 3. strong lambda shock, 4. inclined barrel shock, 5. Mach disk, 6. separation bubble.

where areas with values greater than zero are classified as vortices. Figure 4.1 shows the shock structures of the JICF using a numerical schlieren (magnitude of the density gradient) and Figure 4.2 shows the vortical structures of the JICF using iso-surfaces of the Q-criterion.

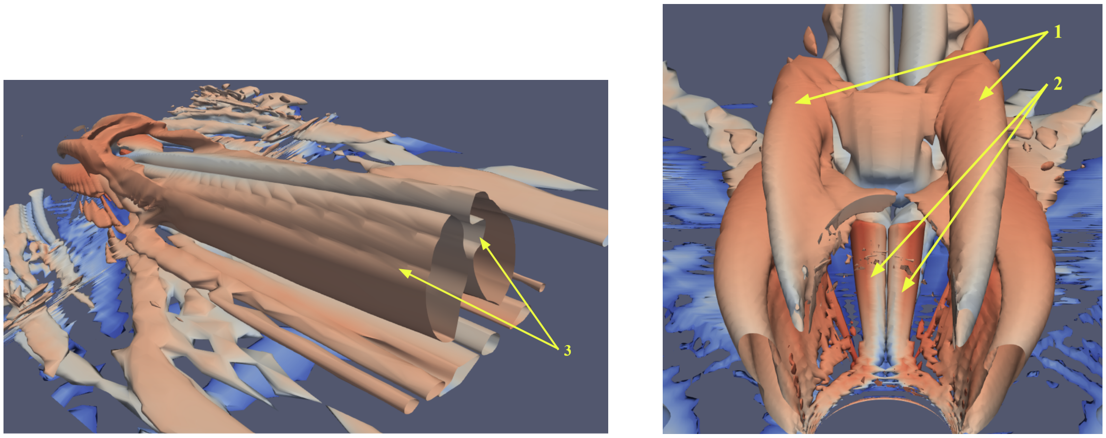

Figure 4.2: Iso-contours of Q-criterion downstream of jet exit colored by instantaneous velocity depicting the main vortex structures: 1. barrel shock and Mach disk shear layer vortices, 2. Kelvin-Helmholtz instability shear layer vortices, 3. CVP.

The crossflow travels from the inlet to the jet exit, where it encounters the jet as an obstacle and forms a bow shock in front of it. There is also a recirculation region that forms just upstream of the jet that induces compression waves, which converge together into a strong separation shock. This shock then acts as a ramp for the crossflow which creates compression waves that form a weak separation shock upstream of the strong separation shock. Upon exiting the nozzle, the sonic jet tries to push through the crossflow and expands creating an inclined barrel shock with a Mach disk at the end. The fluid that passes through the barrel shock and Mach disk produces a shear layer, which rolls up into a pair of vortices. These vortices detach from the jet and combine with the other shear layer originating from the Kelvin-Helmholtz instabilities near the jet exit to form the CVP downstream. This pair of vortices is the dominant flow structure downstream of the jet, as shown in the left side of Figure 4.2. The aforementioned flow physics are visualized and labeled in Figure 4.1 and 4.2.

Figure 4.3 shows the contour of the streamwise skin friction coefficient on the flat plate (bottom wall) of the domain. It is defined

$$C_f \equiv \frac{\mu_w}{\rho_\infty U_\infty^2} \frac{\partial \widetilde{u}}{\partial y}, \tag{4.2}$$

where μ_w is the viscosity near the wall, $\widetilde{u}$ is the time-averaged streamwise component of velocity, ρ_∞ is the freestream density, and U_∞ is the freestream velocity. Upon visual inspection of the contour, the skin friction decreases upstream of the jet due to the separation region from the boundary layer approaching the jet and interacting with the shock structures. However, the flow becomes stagnant just upstream of the jet which results in a region with a low skin friction coefficient. The sides of the jet have a high skin friction coefficient, due to the acceleration of the crossflow passing by the jet. This region extends downstream, following the shape of a horseshoe until about $x = 3.5D$. There is a small region about $x = 5D$ downstream of the jet that has a higher skin friction coefficient.

Figure 4.4 shows a three-dimensional perspective of the time-averaged flow field of the JICF. The central plane (left) shows the normalized pressure contours, the horizontal plane (bottom) shows the Mach contours, and the cross-plane (right) shows the normalized streamwise velocity contours. Both the central

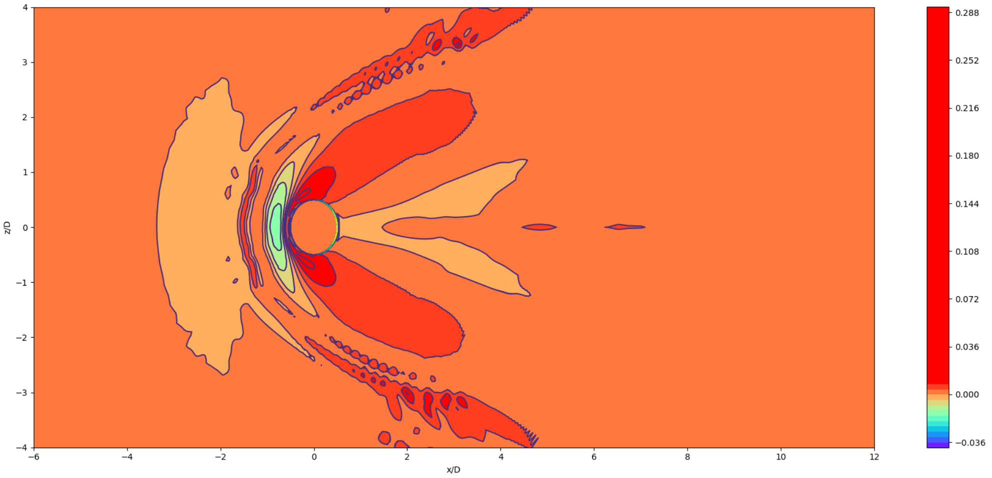

Figure 4.3: Streamwise component of the skin friction coefficient in the central plane on the flat-plate.

and cross-planes also have streamlines projected onto their surfaces to show the motion of the fluid within those planes. These streamlines show the different flow physics such as the upstream recirculation region, high pressure just behind the bow shock and at the upstream near-wall region causing an adverse pressure gradient. It is this adverse pressure gradient that causes the separation of the crossflow boundary layer, including a separation shock above and upstream of the separation bubble. There is also a low-pressure region downstream of the jet, causing reverse flow and thus a recirculation zone near the wall. The streamlines on the central plane show that the jet quickly bends due to the barrel shock and Mach disk. As the flow is turning, there is a source point observed in the near-wall region which is also found by [25] [26] for an incompressible JICF. This occurs due to the reattachment of the crossflow after it finishes traveling around the jet. The cross-plane streamlines show the CVP which is the dominant structure

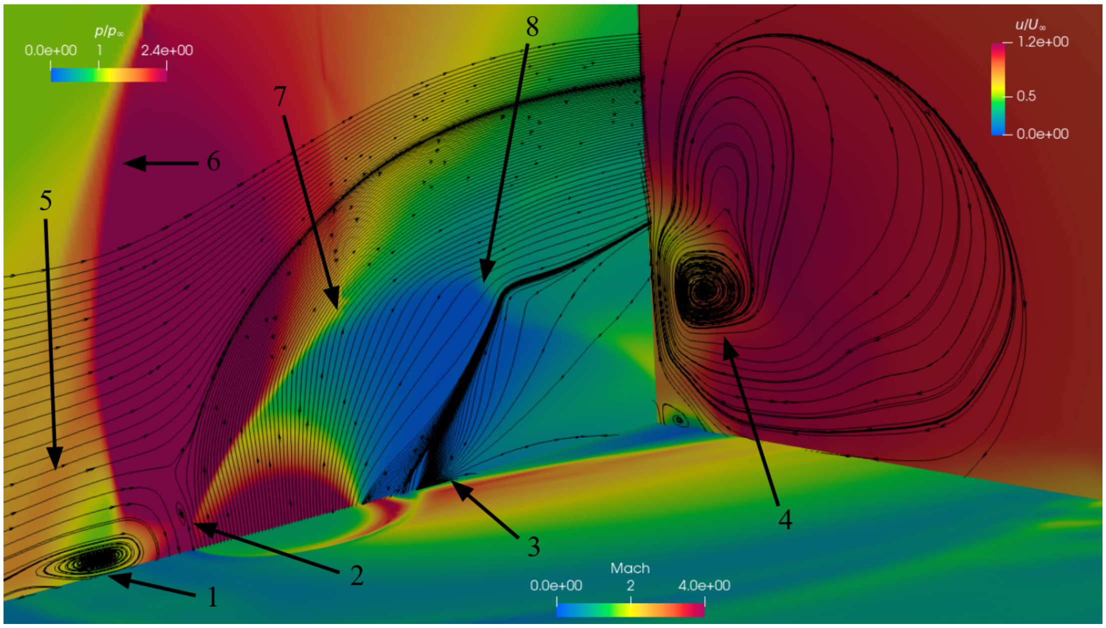

Figure 4.4: Three-dimensional perspective of the time-averaged flow field near the jet exit depicting some flow structures: 1. upstream separation vortex, 2. hovering vortex just upstream of jet, 3. downstream source point, 4. CVP, 5. separation shock, 6. bow shock, 7. inclined barrel shock, 8. Mach disk.

downstream of the jet. There is also another pair of vortices near the downstream wall indicated by the streamlines on the cross-plane.

4.2 Comparison to Experiments

The time-averaged Mach number on the central plane ($z/D = 0$) of the domain for BPANS with $f_k = 0.2$ is given in Figure 4.5a and compared to the LES [5] and experimental [32] data in Figure 4.5b and 4.5c, respectively. Upon close observation, there is a clear difference between the Mach number distribution of the boundary layer in the crossflow. This difference is that the BPANS results have a slightly thicker boundary layer when compared to the LES and experimen-

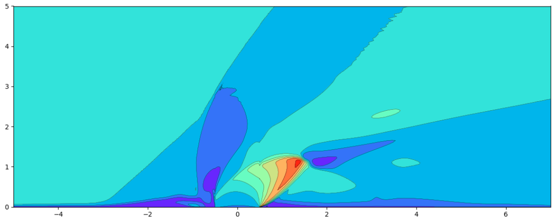

(a) $f_k = 0.2$ BPANS

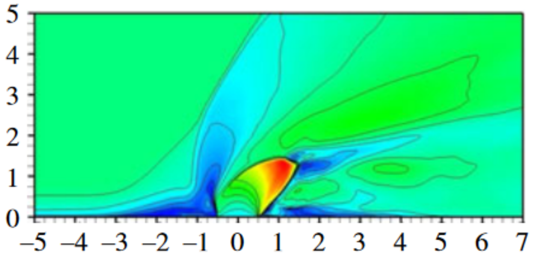

(b) Turbulent inflow refined LES [5]

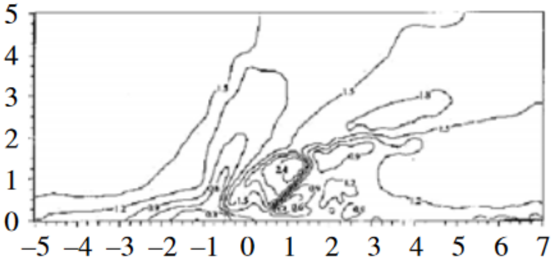

(c) Experiment [32]

Figure 4.5: Time-averaged Mach number contour in the central plane.

tal results. There is also a slight difference in the shape and inclination angle of the barrel shock, along with the mach disk. These differences result from the lack of a fully developed boundary layer in the crossflow inlet, as done in [5] for both laminar and turbulent cases. Other than this, the BPANS results are qualitatively similar to the experimental results. Contours of the streamwise velocity in the central plane are given in Figure 4.6a for BPANS, which is qualitatively similar to the LES [5] and experimental results [32] in Figure 4.6b and 4.6c, respectively.

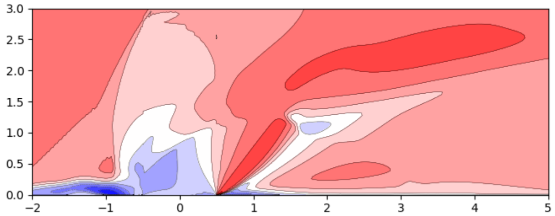

(a) $f_k = 0.2$ BPANS

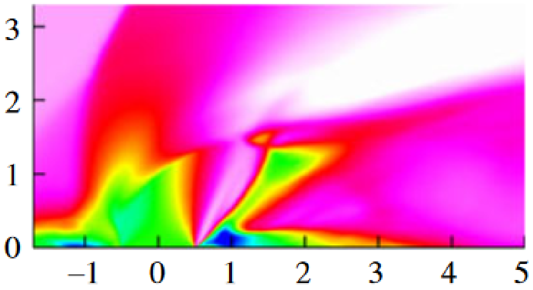

(b) Turbulent inflow refined LES [5]

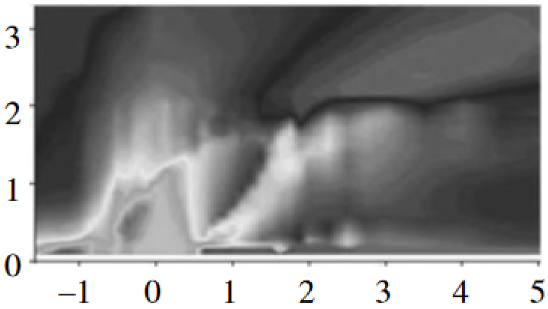

(c) Experiment [32]

Figure 4.6: Time-averaged streamwise velocity contour in the central plane.

The distribution of pressure on the flat plate for the JICF is given in Figure 4.7. The BPANS results show good agreement with both the turbulent inflow refined LES and experimental data. The trajectory of the jet is also studied, which is defined as the streamline that passes through the center of the jet exit. Figure 4.8 compares the BPANS trajectory against the turbulent inflow refined LES and experimental data which shows a good agreement. At $x/JD = 2$ downstream, BPANS jet trajectory hits a height of $y/JD \approx 1.33$ which is slightly shorter than

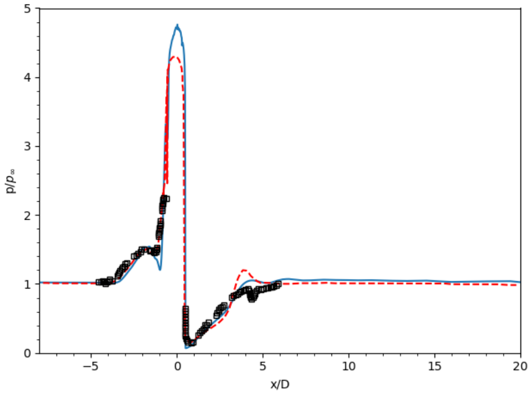

Figure 4.7: Time-averaged wall pressure distribution along central plane. The solid blue line is the $f_k = 0.2$ BPANS data, the dashed red line is the turbulent inflow refined LES data [5] and the symbols are experimental data [7].

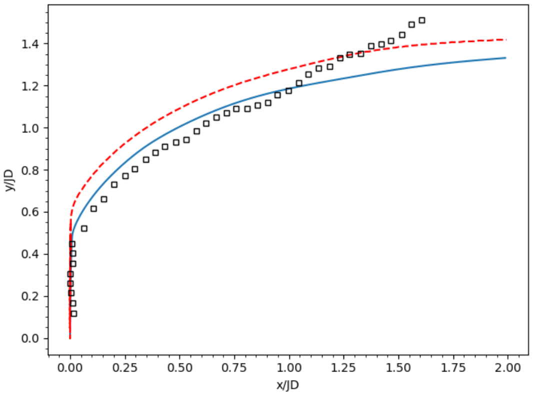

Figure 4.8: Jet trajectory scaled by jet momentum flux ratio. The solid blue line is the $f_k = 0.2$ BPANS data, the dashed red line is the turbulent inflow refined LES data [5] and the symbols are experimental data [14].

the LES jet trajectory height of $y/JD \approx 1.42$. The BPANS jet trajectory also has a better agreement with the experimental data until $x/JD \approx 1.0$ than the LES jet trajectory.

The streamwise and wall-normal velocity profiles are extracted at four locations on the central plane downstream of the jet exit in Figure 4.9: $2D$, $3D$, $4D$, and $5D$. The results show good agreement with the experimental data and the different LES simulations with laminar and turbulent inflow profiles, along with a refined grid for the turbulent inflow LES case.

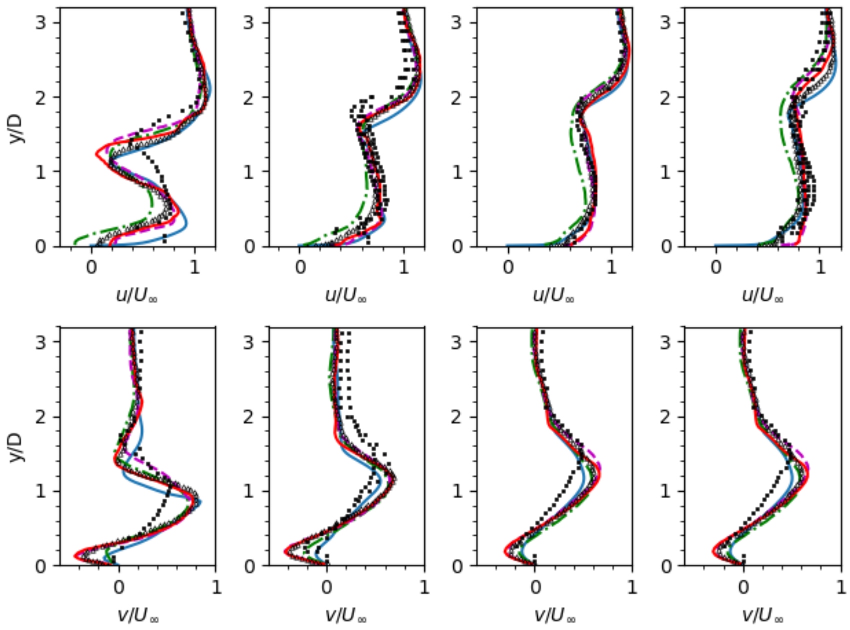

Figure 4.9: Time-averaged velocity profiles at $x/D = 2$, $x/D = 3$, $x/D = 4$, and $x/D = 5$. The solid blue line is BPANS data, dot dash green line is the laminar inflow LES data [5], dotted magenta line is the turbulent inflow LES data [5], the solid red line is the turbulent inflow refined LES data [5], the filled symbols are experimental data from [32], and the hollow symbols are LES data from [18].

4.3 Variation of the Filter Control Parameter

The filter control parameter f_k is varied to investigate how it affects the streamwise and wall-normal velocity profiles, along with the Reynolds stress profiles, downstream of the jet exit. Figure 4.10 depicts the velocity profiles for the three different cases. As f_k is decreased to 0.2, the trends stay consistent and the local extrema have better agreement with the experimental [32] and LES data

[18]. There is a larger deviation between the $f_k = 0.5$ and $f_k = 0.3333$ cases than the $f_k = 0.3333$ and $f_k = 0.2$ cases, indicating that the $f_k = 0.3333$ case may be enough to resolve the flow in the area of interest.

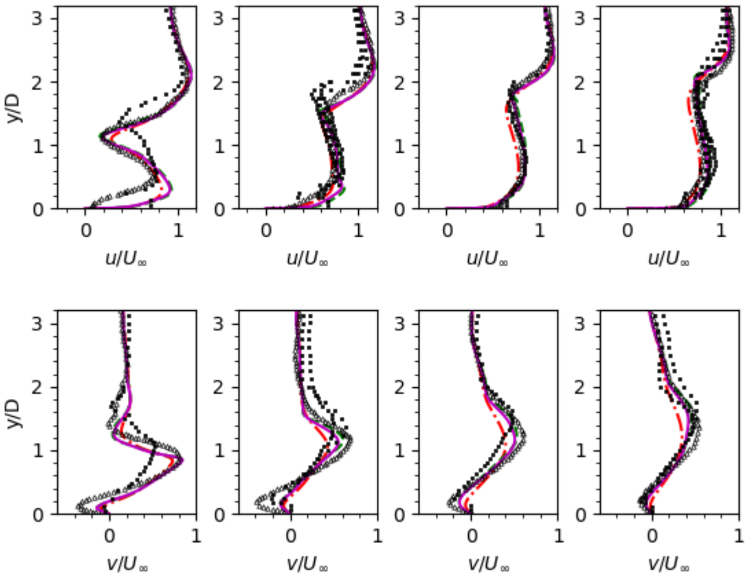

Figure 4.10: Time-averaged velocity profiles at $x/D = 2$, $x/D = 3$, $x/D = 4$, and $x/D = 5$ for f_k of 0.5, 0.3333, and 0.2. The dashed dotted red line is $f_k = 0.5$, the dashed green line is $f_k = 0.3333$, the solid magenta line is $f_k = 0.2$, the filled symbols are experimental data from [32], and the hollow symbols are LES data from [18].

Chapter 5. Conclusions

The extension of the Blended Partially-Averaged Navier-Stokes (BPANS) model to variable-density flow has been presented. The new model was derived from the existing $(k-\omega)$ and $(k-\epsilon)$ PANS models using the approach of Menter with the assumption of a variable density. The results of numerical simulations for the supersonic jet-in-crossflow (JICF) problem were conducted and compared to LES and experimental data.

The variable-density BPANS model demonstrated the ability to resolve the main physics of the supersonic JICF problem. The shock structures, shear layers, and counter-rotating vortex pair (CVP) were visualized and a discussion was presented about how they dominate the physics of the problem. Variable-density BPANS also demonstrated the ability to accurately capture the mean streamwise and wall-normal velocity profiles when compared to higher fidelity LES and experimental data. The wall pressure on the flat-plate of the domain, as well as the jet trajectory, are also accurately predicted compared to the LES and experimental data.

The filter control parameter f_k was varied for the supersonic JICF problem. The value of $f_k = 0.2$ had the best agreement with the LES and experimental data, but $f_k = 0.3333$ only slightly deviated from the $f_k = 0.2$ curves. As f_k was lowered, the variable-density BPANS model showed better agreement with the experimental data near local extrema.

References

[1] A. Ben-Yakar, M. G. Mungal, and R. K. Hanson. Time evolution and mixing characteristics of hydrogen and ethylene transverse jets in supersonic crossflows. *Physics of Fluids*, 18(2):026101, 02 2006.

[2] Steven Beresh, Rocky Erven, John Henfling, and Russell Spillers. Penetration of a transverse supersonic jet into a subsonic compressible crossflow. *Aiaa Journal - AIAA J*, 43:379–389, 02 2005.

[3] Steven J Beresh, John F. Henfling, Rocky Erven, and Russell W. Spillers. Crossplane velocimetry of a transverse supersonic jet in a transonic crossflow. 1 2006.

[4] Steven J Beresh, John F Henfling, and Rocky J Erven. Surface measurements of a supersonic jet in subsonic compressible crossflow for the validation of computational models. 10 2002.

[5] Xiaochuan Chai, Prahladh S. Iyer, and Krishnan Mahesh. Numerical study of high speed jets in crossflow. *Journal of Fluid Mechanics*, 785:152–188, 2015.

[6] Rocky J Erven, Steven Jay Beresh, Russell W Spillers, and John Francis Henfling. Turbulent characteristics of a transverse supersonic jet in a subsonic compressible crossflow. 6 2004.

[7] D. E. Everett, M. A. Woodmansee, J. C. Dutton, and M. J. Morris. Wall pressure measurements for a sonic jet injected transversely into a supersonic crossflow. *Journal of Propulsion and Power*, 14(6):861–868, 1998.

[8] Joel H. Ferziger and Milovan Perić. *Computational Methods for Fluid Dynamics*. Springer, 4th edition, 2020.

[9] Abdelkader Frendi and Christopher Harrison. Partially averaged navier-stokes: A (k-ω)/(k-ϵ) bridging model. *Fluids*, 5(3), 2020.

[10] T. F. Fric and A. Roshko. Vortical structure in the wake of a transverse jet. *Journal of Fluid Mechanics*, 279:1–47, 1994.

[11] Geuzaine, Christophe and Remacle, Jean-Francois. Gmsh.

[12] Sharath S. Girimaji. Partially-Averaged Navier-Stokes Model for Turbulence: A Reynolds-Averaged Navier-Stokes to Direct Numerical Simulation Bridging Method. *Journal of Applied Mechanics*, 73(3):413–421, 11 2005.

[13] Harish Gopalan, Stefan Heinz, and Michael K. Stöllinger. A unified rans–les model: Computational development, accuracy and cost. *Journal of Computational Physics*, 249:249–274, 2013.

[14] M. R. Gruber, A. S. Nejad, T. H. Chen, and J. C. Dutton. Mixing and penetration studies of sonic jets in a mach 2 freestream. *Journal of Propulsion and Power*, 11(2):315–323, 1995.

[15] G. HALLER. An objective definition of a vortex. *Journal of Fluid Mechanics*, 525:1–26, 2005.

[16] Antony Jameson. Origins and further development of the jameson–schmidt–turkel scheme. *AIAA Journal*, 55:1–23, 03 2017.

[17] W.P Jones and B.E Launder. The prediction of laminarization with a two-equation model of turbulence. *International Journal of Heat and Mass Transfer*, 15(2):301–314, 1972.

[18] Soshi Kawai and Sanjiva K. Lele. Large-eddy simulation of jet mixing in supersonic crossflows. *AIAA Journal*, 48(9):2063–2083, 2010.

[19] Sunil Lakshmipathy and Sharath Girimaji. *Partially-averaged Navier-Stokes method for turbulent flows: k-w model implementation.*

[20] J. McDaniel, J. C. Graves. A laser-induced-fluorescence visualization study of transverse, sonic fuel injection in a nonreacting supersonic combustor. *Journal of Propulsion and Power*, 4(6):591–597, 1986.

[21] B. K. McMillin, J. M. Seitzman, and R. K. Hanson. Comparison of no and oh planar fluorescence temperature measurements in scramjet model flowfield. *AIAA Journal*, 32(10):1945–1952, 1994.

[22] F. R. Menter. Two-equation eddy-viscosity turbulence models for engineering applications. *AIAA Journal*, 32(8):1598–1605, 1994.

[23] Florian R. Menter. Zonal two equation k-w turbulence models for aerodynamic flows. 1993.

[24] Pierce C. A. Jr Craven C. E. Morkovin, M. V. nteraction of a side jets with a supersonic main stream. *Bulletin 35, Engineering Research Institute, University of Michigan*, 1952.

[25] SUMAN MUPPIDI and KRISHNAN MAHESH. Study of trajectories of jets in crossflow using direct numerical simulations. *Journal of Fluid Mechanics*, 530:81–100, 2005.

[26] SUMAN MUPPIDI and KRISHNAN MAHESH. Direct numerical simulation of passive scalar transport in transverse jets. *Journal of Fluid Mechanics*, 598:335–360, 2008.

[27] S. Pai. *Viscous Flow Theory, II–Turbulent Flow.* Van Nostrand, New York, 1956.

[28] Francisco Palacios, Michael Colonno, Aniket Aranake, Alejandro Campos, Sean Copeland, Thomas Economon, Amrita Lonkar, Trent Lukaczyk, Thomas Taylor, and Juan Alonso. Stanford university unstructured (su2): An open-source integrated computational environment for multi-physics simulation and design. 01 2013.

[29] F. S. Pereira, F. F. Grinstein, D. M. Israel, R. Rauenzahn, and S. S. Girimaji. Partially averaged navier-stokes closure modeling for variable-density turbulent flow. *Phys. Rev. Fluids*, 6:084602, Aug 2021.

[30] Stephen B. Pope. *Turbulent Flows.* Cambridge University Press, 2000.

[31] L. Prandtl. 7. bericht über untersuchungen zur ausgebildeten turbulenz. *ZAMM - Journal of Applied Mathematics and Mechanics / Zeitschrift für Angewandte Mathematik und Mechanik*, 5(2):136–139, 1925.

[32] Juan Gabriel Santiago and J. Craig Dutton. Velocity measurements of a jet injected into a supersonic crossflow. *Journal of Propulsion and Power*, 13(2):264–273, 1997.

[33] François G. Schmitt. About boussinesq's turbulent viscosity hypothesis: historical remarks and a direct evaluation of its validity. *Comptes Rendus Mécanique*, 335(9):617–627, 2007.

[34] J. SMAGORINSKY. General circulation experiments with the primitive equations: I. the basic experiment. *Monthly Weather Review*, 91(3):99 – 164, 1963.

[35] Philippe Spalart, W-H Jou, Michael Strelets, and Steven Allmaras. Comments on the feasibility of les for wings, and on a hybrid rans/les approach. 01 1997.

[36] Dudley Brian Spalding, Andrei Nikolaevich Kolmogorov, Lev Davydovitch Landau, Piotr Leonidovich Kapitza, Julian Charles Roland Hunt, Owen Martin Phillips, and David Williams. Kolmogorov's two-equation model of turbulence. *Proceedings of the Royal Society of London. Series A: Mathematical and Physical Sciences*, 434(1890):211–216, 1991.

[37] Girimaji S.S. Suman, S. On the invariance of compressible navier–stokes and energy equations subject to density-weighted filtering. *Flow, Turbulence and Combustion*, 85:383–396, 6 2010.

[38] William Sutherland. Lii. the viscosity of gases and molecular force. *The London, Edinburgh, and Dublin Philosophical Magazine and Journal of Science*, 36(223):507–531, 1893.

[39] S. Trapier, S. Deck, and P. Duveau. Delayed detached-eddy simulation and analysis of supersonic inlet buzz. *AIAA Journal*, 46(1):118–131, 2008.

[40] H.G. Weller, Gavin Tabor, Hrvoje Jasak, and Christer Fureby. A tensorial approach to computational continuum mechanics using object orientated techniques. *Computers in Physics*, 12:620–631, 11 1998.

[41] David C. Wilcox. Reassessment of the scale-determining equation for advanced turbulence models. *AIAA Journal*, 26(11):1299–1310, 1988.

[42] D.C. Wilcox. *Turbulence Modeling for CFD. 3rd Edition.* DCW Industries, 2006.